



# OPEN Vibration response of piles at different distances induced by shield tunneling in hard rock strata

You Wang<sup>✉</sup>, Yue Ma, Rui Wang, Bosong Ding & Siyuan Yu

Excavation of subway tunnels in hard rock generates strong vibration waves that pose potential risks to the stability of surrounding structures. In this study, the discrete element method-finite difference method (DEM-FDM) coupling was adopted to build the model of tunnel structure-rock-pile, which was validated by field monitoring data. Then, the vibration response of piles under various pile-tunnel spacings was analyzed, revealing the occurrence of vibration peak rebound phenomena within certain distance ranges. The range of vibration effects was categorized. Furthermore, in shield tunneling construction, the energy induced by vibrations was mainly concentrated within the 50 Hz range. Low-frequency vibrations result in a wider effect range. The study also demonstrated that within a 1d (tunnel diameter) range of the pile-tunnel spacing, the vibration induced by shield tunneling construction had a more significant effect. As the pile-tunnel spacing increased, the piles transitioned from being subjected to bending forces to experiencing bending-shear forces. Finally, the vibration effects on the existing piles were evaluated under field working conditions. It also provided suggestions for construction based on the effects and laws of the pile dynamic response.

**Keywords** Hard rock, Shield tunnel, Field monitoring, FDM-DEM coupling, Pile-tunnel spacing, Dynamic response

With population growth and urban expansion, urban infrastructure is facing increasing challenges. In order to alleviate urban traffic congestion, more and more cities are choosing to build metro systems. According to statistics, by the end of 2023, the operating mileage of urban metro systems in China had reached 9915.6 km<sup>1</sup>. However, urban subway construction not only needs to face complex geological conditions, pipelines, buildings and other underground environments, but also the vibration problems caused by the construction process cannot be ignored.

Shield machine is widely used in the construction of subway tunnels in central urban areas due to its high construction speed, safe construction environment and minimal ground disruption<sup>2–4</sup>. However, the shield cutterhead often generates intense vibration waves in the process of cutting rock, which propagate through the strata to the surface and adjacent structures. Many engineering practices showed that tunnel excavation inevitably affected the operational status of adjacent buildings. Among them, the vibrations generated by the shield tunneling machine during the excavation process induced structural resonance in nearby buildings<sup>5,6</sup>. Additionally, the noise generated by the vibrations also impacted individuals' physical health and work-life in surrounding buildings<sup>7,8</sup>. In certain construction projects, it was observed that the vibration acceleration amplitude of the main beam of the shield system during tunneling operations reached up to 4 g. Moreover, if the vibrations at the cutterhead, drive unit, and main beam were too severe, they could even lead to the fracture of the connecting bolts between the cutterhead and the main drive, severely reducing construction efficiency<sup>9,10</sup>. Therefore, actively conducting research on the impact of vibration during urban subway tunnel shield construction and control technologies was of practical and significant importance.

In 1984, Nelson et al. conducted a detailed monitoring of the vibration generated by the shield machine in hard rock<sup>11</sup>. This was the first time that scholars began to pay attention to and measure the vibration during the shield construction process. In 2020, Namli and Aras's on-site monitoring of buildings between 2 tunnels in Istanbul found that the amplitude of the buildings increased by a factor of four as the shield machine passed by<sup>12</sup>. The mechanism of vibration propagation was a prerequisite for vibration control and mitigation. Scholars from various countries researched the mechanisms of vibration impact to reduce the hazards caused by vibrations during shield tunneling. Tian and Jian suggested that the vibrations caused by shield tunneling were related to distance, proposing that the vibrations decreased exponentially with increasing distance<sup>13,14</sup>. Guo measured

College of civil engineering, Central South University, 410075 Changsha, Hunan, China. ✉email: [youwang1920@csu.edu.cn](mailto:youwang1920@csu.edu.cn)

and analyzed the vibration response during shield tunneling in the Lanzhou gravel-sand strata and found that the vibration levels at different frequency bands exhibited varying degrees of local amplification, which might have been related to the dominant frequency of the site<sup>15</sup>. Wang Xin et al. proposed a quantitative indicator for the main influencing factors of shield vibrations: the weighted dynamic elastic modulus of the strata at the tunnel face, arguing that the stiffness of the strata at the excavation site was the primary indicator affecting the strength of the vibrations<sup>16</sup>. Liu et al. found that in homogeneous soft soil foundations (HSG), the vibration intensity was low and stable; whereas, under the influence of mixed foundations (MFC), high-frequency strong vibrations occurred<sup>17</sup>. Xu Riqing et al. believed that the main influencing factors of shield vibrations, in addition to the properties of the soil surrounding the tunnel, included the thrust and torque of the cutterhead and other tunneling parameters, which were also crucial<sup>18</sup>.

In recent years, the research on the vibration response of shield tunneling was mainly based on field monitoring and numerical simulation. From 2013 to 2015, Wang Xin et al. established a dynamic model of tunnel structure-rock-structure interaction using on-site monitoring data and employed Z-soil finite element analysis software. It laid the groundwork for numerical simulation research on shield construction vibrations<sup>19–21</sup>. Wang et al. used FLAC3D software for shield tunnel construction simulation to study the effect of shield construction vibration on soil disturbance in liquefiable strata<sup>22</sup>. Araz et al. used FLAC 3D software to study the vibration response of liquefiable shallow foundations and explored the seismic performance of DMS in liquefiable shallow foundations<sup>23</sup>. Gupta et al. conducted a parametric study on the coupling between tunnels and surrounding rock, providing a theoretical reference for the coupling issues in numerical simulations<sup>24</sup>. Lu et al. established a vibration acceleration prediction model based on excavation parameters using the GA-BP neural network algorithm. The vibrations generated during shield tunneling not only propagate through the strata but also induce responses in nearby buildings<sup>25</sup>. Guo et al. analyzed the effect of shield construction vibration on frame structures by inputting measured acceleration time courses through ABAQUS software<sup>26</sup>. Wu et al. used a combination of on-site monitoring and three-dimensional fully coupled linear dynamic finite element modeling to study the effects of vibration on existing buildings with different foundation types. And showed that hard rock tunnel excavation may lead to building vibration exceeding the standard limits<sup>16</sup>. Yang et al. analyzed the response of pile groups induced by tunnel excavation using a coupled ALEM-FEM-BEM method<sup>27</sup>. Lai et al. simulated the shield tunnel boring process under different conditions using a three-dimensional finite element model and combined it with on-site measurements to derive the deformation law of the city wall structure and the change rule of the surface settlement trough<sup>28</sup>.

Most studies about subway tunnel vibration have concentrated on the effects generated during operation<sup>29–32</sup>. However, the vibration acceleration caused by shield tunneling in hard rock is several times higher<sup>16</sup>. At present, research on shield construction vibrations primarily concentrates on their propagation in geological strata and the impact on the upper structures of ancient buildings, residential buildings, etc. However, there has been relatively little research on building foundations, such as pile foundations. Pile foundations are closer to the vibration source than the upper structures of buildings, and initial damage to them is often difficult to detect. Therefore, once resonance or damage occurs, the consequences can be severe. Consequently, it is necessary to study and analyze this factor.

To investigate the effects of shield tunnel construction vibrations on adjacent piles, the DEM-FDM coupling method was applied in this study. It combines the advantages of particle flow in simulating geotechnical materials with the suitability of finite element mesh for dynamic analysis to establish a model of the tunnel structure-rock-piles. Taking the shield tunnel of Jinan Metro Line 4 as a case, this paper simulated different pile-tunnel spacing working conditions during shield tunneling to analyze the vibration patterns of piles. Based on this analysis, the scope of vibration influence was delineated. Furthermore, the time-frequency characteristics and energy distribution patterns of the vibration signals were revealed by continuous wavelet transform and wavelet packet analysis. The degree of shield construction vibration on piles was evaluated based on field monitoring data, providing a reference for the excavation of shield tunnels.

## Methodologies

### Field monitoring

The geological formation in the vibration monitoring section is mainly moderately weathered limestone, with occasional layers of silty clay and sandy soil. The tunnel is buried at a depth of 10.9 m. directly above the tunnel is a major urban road. Vibration monitoring was carried out between 21:00 and 23:30 to minimize the effect of external background noise. The monitoring was carried out in two sessions, each lasting 20–30 min.

The vibrations generated during shield tunneling are mainly caused by the cutterhead cutting through the rock. Therefore, the closer the sensors are to the vibration source, the more accurate the measurements. However, the area near the cutterhead contains slurry, rock fragments, and other debris that could potentially damage the sensors. As a result, four sets of sensors were installed on both sides of the first segment of the lining behind the cutterhead in this test, and the measured vibration accelerations were treated as the vibration source. Additionally, monitoring points were installed on the ground surface directly above the tunnel excavation face to collect data on displacement, velocity, and acceleration after the vibrations generated by the shield tunneling propagate to the surface, as shown in (Fig. 1).

The main technologies used to monitor the tunnel interior include accelerometers, smart sensors, seismometers, acoustic emission devices, infrared thermography, etc<sup>33</sup>. To obtain vibration signals during the shield tunneling process, sensitive sensor equipment was used to record vibrations from the tunnel lining and surface during the start-up, excavation, and completion phases of tunneling. As seen in Fig. 1, monitoring points were set on the first segment of the lining behind the cutterhead and the ground surface directly above the tunnel. The sensor model is WTVB01-BT50, which uses advanced digital filtering technology to reduce measurement noise effectively. It offers an output rate of up to 1000 Hz, providing comprehensive data including three-axis

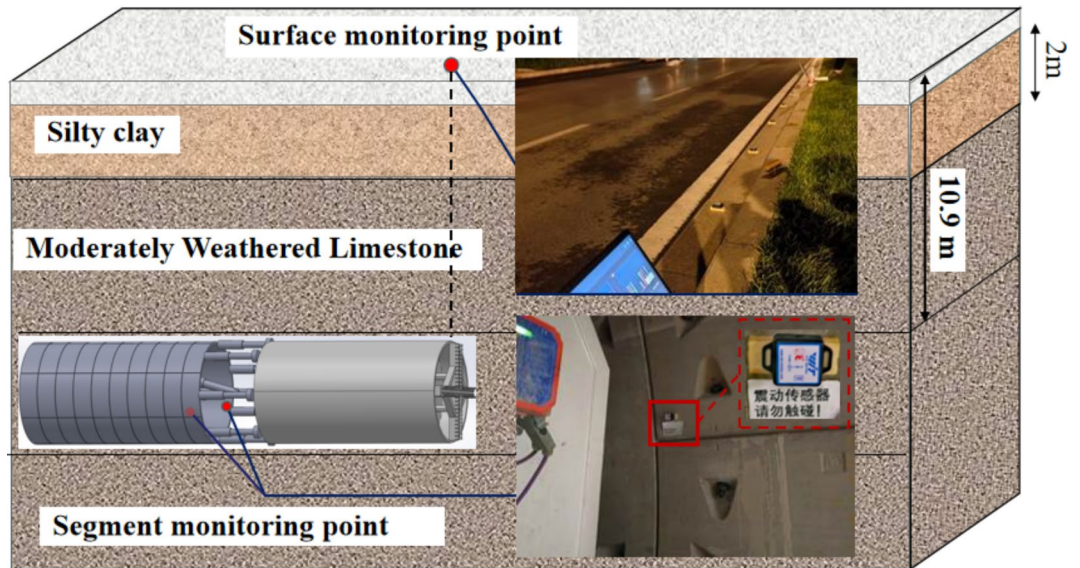


Fig. 1. Arrangement and monitoring of sensors.

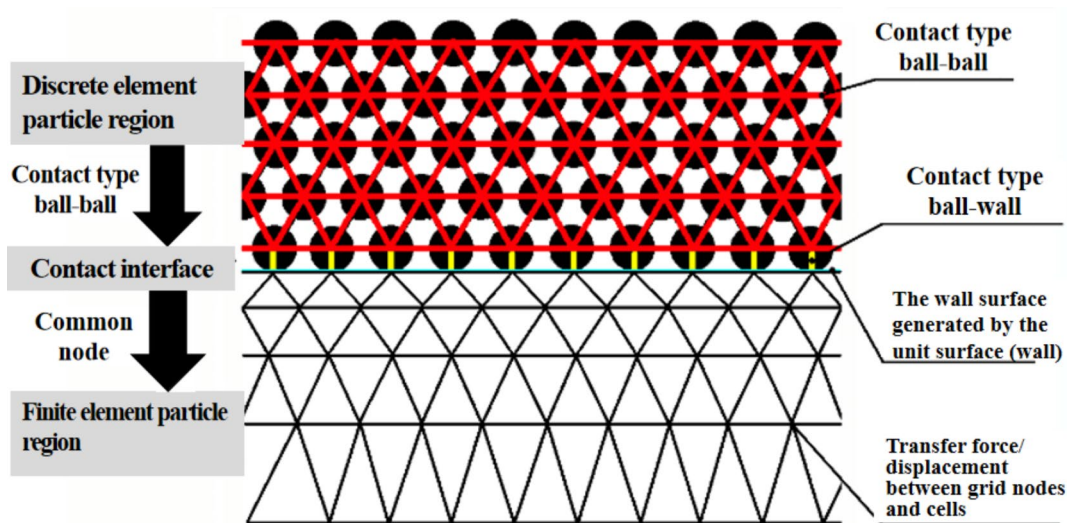


Fig. 2. DEM-FDM coupling principle schematic.

displacement, three-axis velocity, and three-axis frequency. The vibration displacement and velocity range are  $\pm 30,000 \mu\text{m}$  and  $\pm 50 \text{ mm/s}$  respectively, with an accuracy of  $< \text{FS} \pm 5\%$ . Considering that the vibrations generated by tunnel shield construction are generally within a few hundred hertz, the sampling frequency within the tunnel was set to 300 Hz. The dominant frequencies at the surface are primarily below 100 Hz. Therefore, the surface sampling frequency was set to 200 Hz, which satisfies the Nyquist sampling theorem.

### DEM-FDM coupling

The model employed PFC 2D discrete element software for simulating the accumulation of soil layers, and utilized FLAC 2D finite difference software for modeling and mesh generation of tunnels and piles.

In order to enable the discrete element particles and finite difference grids to smoothly transfer the mechanical and physical properties, the model adopted the interface coupling method<sup>34,35</sup>. A PFC model component “Wall” was set on the surface of FLAC model elements (zones or structural units) to serve as a medium for exchanging and transferring coupling variables. This enabled the realization of a continuous-discontinuous coupling process, as illustrated in Fig. 2. By generating walls corresponding to nodes on the finite difference grid surface, discrete element particles can transfer forces and displacements to the interior of grid nodes and elements through these walls. The discrete elements of the contact zone and finite difference units mutually provide boundary conditions for each other. From the perspective of coordinating spatial unit size and computational time step length, a

coupled computational platform integrating discrete element method (DEM) and finite difference method (FDM) was constructed using Newton's second law and explicit Lagrangian algorithm.

The function of coupled logic is to determine the equivalent force system at the vertices of a triangular surface through contact forces and moments of wall. These forces, along with stiffness, are transmitted to the mesh and nodes<sup>36,37</sup>. Figure 3 shows a coupled element, where the "Wall" used in PFC calculations are considered as  $n$  triangular faces  $F_i (i = 1, 2, 3, \dots, n)$  after grid partitioning. Assuming contact between a sphere and a triangular wall,  $C$  is the contact point, and  $CP$  is the point on the wall closest to point  $C$ . Extrapolation from  $CP$  to the vertices of the triangle is done using the barycentric interpolation method.  $V_k^{(i)} (i = 1, 2, 3)$  denotes the positions of the triangle vertices. By connecting the three vertices to  $CP$ , three triangles are formed, with area  $A_i (i = 1, 2, 3)$ , and the total area of the three triangular faces is given by  $A = A_1 + A_2 + A_3$ .

The vertex weighting factor is defined as the ratio of the area of the triangle relative to the vertex divided by the total area of the triangle,  $\omega_i = A_i/A, \sum \omega_i = 1$ , to ensure that the sum of extrapolated values from  $CP$  to the vertices equals the value at  $CP$ . When the full computation mode is disabled, contact forces and translational stiffness are also extrapolated to the nodes in this manner.

Assuming  $R_i (i = 1, 2, 3)$  as the vector from  $CP$  to each of the three vertices,  $R_i = V_k^{(i)} - CP$ . The force applied at each grid point or node is denoted as  $F_i (i = 1, 2, 3, \dots, n)$ , while the force applied at contact point  $C$  is denoted as  $F$ , and the torque due to the adhesive force at the contact point is denoted as  $M_b$ . Since the contact point  $C$  and the point  $CP$  on the contact plane may not coincide, the total torque acting on the contact plane is:

$$\vec{M} = \vec{M}_b + (C - CP) \times \vec{F} \tag{1}$$

When the full computation mode is active, the coupling scheme determines a fully consistent equivalent force system:

$$\sum_1^3 F_i = \vec{F} \tag{2}$$

$$\sum \vec{R}_i \times \vec{F}_i = \vec{M} \tag{3}$$

$n$  is the unit normal vector to the triangular face, and the shear force vector along the triangular face is denoted as  $F^s$ :

$$\vec{F}^s = \vec{F} \cdot \vec{n} \tag{4}$$

$$\vec{S} = \frac{\vec{F}^s}{\|F^s\|} \tag{5}$$

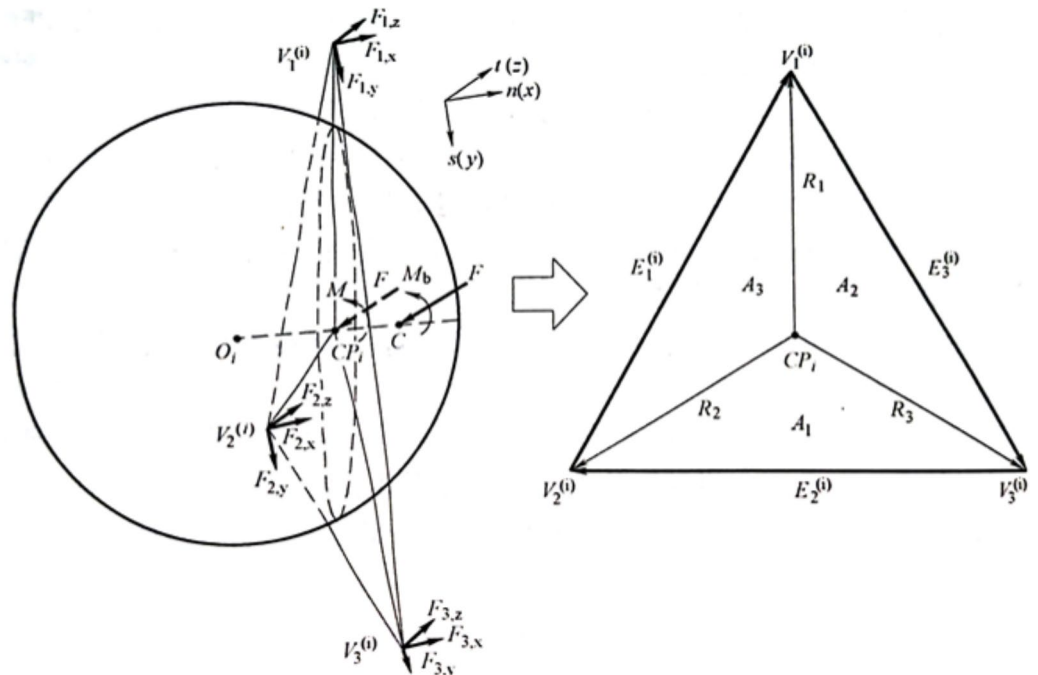


Fig. 3. Transfer of coupled forces.

In the local coordinate system, the direction of the axis aligns with the direction of the normal vector  $n$ , and the direction of the  $y$ -axis aligns with the direction of the shear direction  $s$ . Since the CP point lies on the triangular face,  $R_{i,x} = 0$ . This simplification directly determines the components of vertex force and torque in the  $x$ ,  $y$ , and  $z$  directions in the local coordinate system, denoted as  $F_{i,x}$ ,  $F_{i,y}$  and  $F_{i,z}$ :

$$\sum \vec{F}_{i,x} = \vec{F}_x \quad (6)$$

$$\sum \vec{F}_{i,y} = \vec{F}_y \quad (7)$$

$$\sum \vec{F}_{i,z} = \vec{F}_z = 0 \quad (8)$$

$$\sum (\vec{R}_{i,y} \times \vec{F}_{i,z} - \vec{R}_{i,z} \times \vec{F}_{i,y}) = \vec{M}_x \quad (9)$$

$$\sum (\vec{R}_{i,z} \times \vec{F}_{i,x} - \vec{R}_{i,x} \times \vec{F}_{i,z}) = \vec{M}_y \quad (10)$$

$$\sum (\vec{R}_{i,x} \times \vec{F}_{i,y} - \vec{R}_{i,y} \times \vec{F}_{i,x}) = \vec{M}_z \quad (11)$$

$$\sum F_{i,y} = w_i F_y \quad (12)$$

$$\sum F_{i,z} = 0 \quad (13)$$

Therefore, in FLAC 3D, the contact surface between the continuous and discrete regions of PFC is defined as the wall. During the motion of balls or clumps, the contact forces and contact moments acting on the wall are allocated to the wall vertices using the equivalent force method. The wall vertices are attached to the grid points of solid elements, allowing synchronized motion and transmission of contact forces and moments.

### Project overview

Jinan Metro Line 4, from Shanda Station to Shanshi East Station, is shown in (Fig. 4). Interval out of the Shanda Station, the line travels westward along JingShi Road. The right line tunnels passes under the Agricultural Bank, Wendong Building 5#, and passes adjacent to Wendong Building 3#. The left line passes adjacent to the Judicial Office Building. Both lines tunnel under Yangtouyu Bridge before exiting at Shanshi East Station.

According to the on-site information, the metro line passes beneath and adjacent to multiple residential areas, with hospitals, research institutes, and other facilities distributed along its route. Specifically, the left line passes adjacent to Wendong Building 3# between rings 15 and 36. The horizontal distance between this building and the tunnel is only 2.34, 11.6 m from the tunnel roof. The right line directly passes under Wendong Building 5# between rings 25 and 72, with a distance of 10.6 m from the tunnel roof. The surrounding area consists of densely populated urban main roads, resulting in a relatively high level of risk.

The total length of this section is approximately 525.9 m, with shield tunneling as the construction method. The soil cover thickness over the tunnel roof ranges from 9.5 to 11.7 m. The tunnel's inner diameter is 5.6 m, the outer diameter is 6.2 m, and the segment thickness is 30 cm. The geological profile is depicted in Fig. 5, primarily consisting of fully weathered gabbro, highly weathered gabbro, moderately weathered gabbro and moderately weathered limestone, as detailed in Table 1 for rock layer characteristics.

According to the chart information, the stratum of the line is mainly composed of rock with high strength, which is a hard rock strata. During the construction of the shield machine, the characteristics of the rock strata will result in significant vibrations caused by the advancement of the shield machine. These vibrations can adversely affect the surrounding buildings and may even lead to structural damage to the buildings especially for some special buildings, such as hospitals and old residential areas.

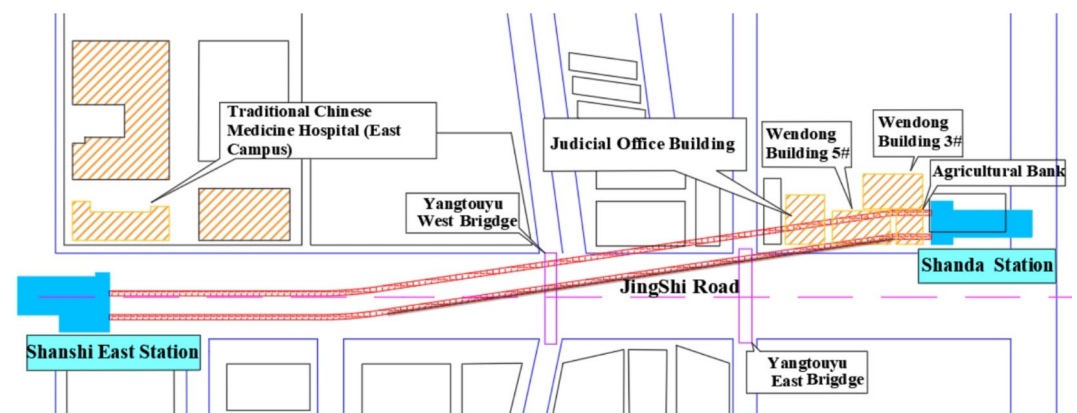
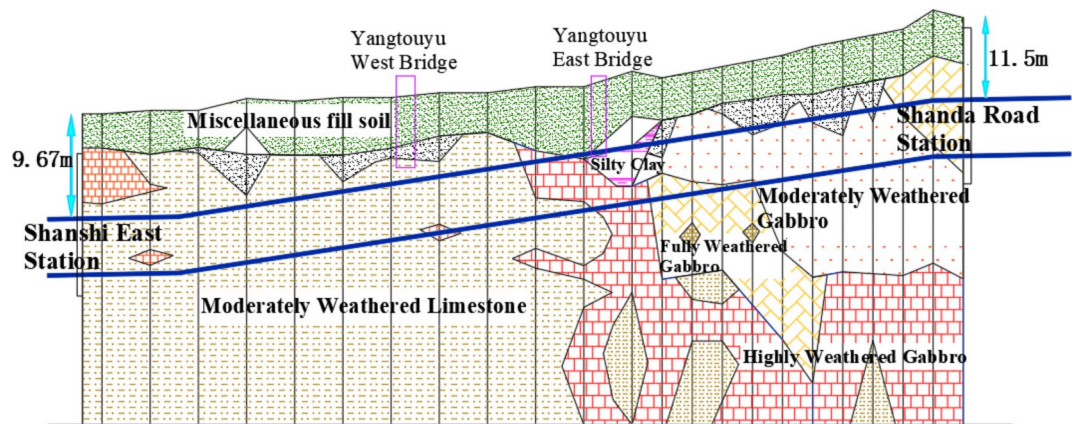


Fig. 4. Route map of Jinan metro line 4 Shan-Shan section.



**Fig. 5.** Rock layer map of Jinan metro line 4 Shan-Shan section.

Stratum	Rock strength
Fully weathered gabbro	RQD = 0–40. Heavy-duty dynamic probing approximately 36.7 blows
Highly weathered gabbro	Heavy-duty dynamic probing approximately 32.34 blows
Moderately weathered gabbro	Natural compressive strength ranges from 10.2 to 28.6 MPa. RQD = 40–95
Moderately weathered limestone	Natural compressive strength ranges from 47.5 to 94.7 MPa. RQD = 85–95

**Table 1.** Characteristics of rock strata in Shan-Shan section of Jinan metro line 4.

## Numerical simulation

### Field monitoring results

In order to obtain the vibration signals during the shield tunneling process, monitoring points were set up on the lining behind the cutterhead for vibration source signal data acquisition. The monitoring data of the shield machine tunneling process was shown in (Fig. 6).

The on-site monitoring lasted for 1 h and was divided into three stages. During the first 300 s, the shield machine was in the initial start-up condition, and minimal vibrations were mainly caused by environmental factors. From 300 s to 1650 s was the excavation process of the shield machine, where the maximum vibration velocity generated by the tunnel excavation reached 3 mm/s, with an average velocity distribution of about 1 mm/s. From 1650 to 2000 s, as the shield tunneling process approached completion, the vibration velocity gradually decreased to less than 0.5 mm/s.

During the model validation process, the surface vibrations caused by tunnel excavation were relatively minor. To facilitate the demonstration of the model's reliability, a segment of the vibration signals with more pronounced intensity during shield tunneling was selected as the vibration source, as illustrated in (Fig. 6). This approach enabled a more effective validation of the model's accuracy.

### Numerical model development

In the case of the Shan-Shan section of Jinan Metro Line 4, a two-dimensional computational geological model with a width of 48 m and a height of 27 m was established as shown in (Fig. 7). The tunnel excavation had an inner diameter of 5.6 m, and the tunnel segments were made of C50 concrete material with a thickness of 0.3 m, based on actual construction conditions. In the geological modeling process, the primary material was moderately weathered limestone, and a linear parallel bond model was used between the particles. The diameter range of the discrete element particles (balls) used to simulate the sedimentary layers was from 4 to 9 centimeters, with the particle size distribution following a Gaussian distribution. Before excavation, the total number of balls was

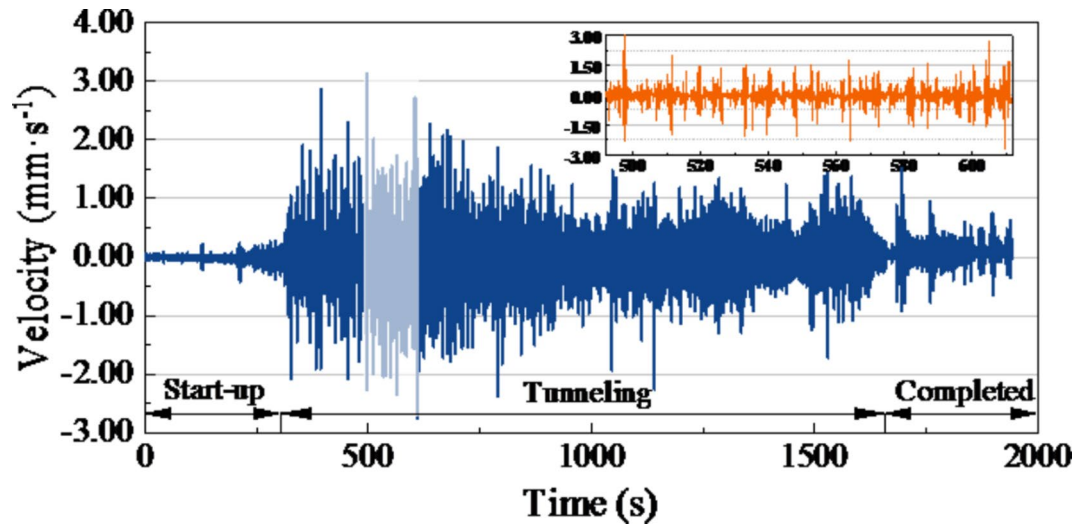


Fig. 6. Monitoring data of vibration velocity of the first segment of tunnel lining.

87,345. According to the engineering specifications, the tunnel was designed to be buried at a depth of -10.9m. The tunnel lining segments and pile were modeled as mesh elements using an elastic constitutive model. The length of the pile foundation was 22.8 meters, and the diameter was 0.6 meters. Due to the simple geometric shapes of the segment and pile, the quadrilateral mesh can be generated using the 'extrusion' module functionality built into the software according to the shapes of the pile foundation and segment. The pile and tunnel segments (zone) interacted with the geological layers (balls) through a generated contact surface (wall-zone), transmitting contact forces and moments to achieve synchronous motion and coupling between discrete elements and finite differences. The bottom of the tunnel segments was positioned 10 m above the bottom boundary of the model, and the tunnel segments were approximately 20 m away from the sides of the model boundaries. The boundary of the stratum accumulation model was defined using wall elements, with fixed constraints applied to the bottom and side surfaces, and the top surface left free, as shown in (Fig. 7a).

After the mesh partitioning was completed, the pile mesh was designated an elastic model with the relevant properties assigned, thereby generating the pile foundation. The pile was then fixed in place to establish the initial equilibrium of the particles. To ensure sufficient equilibrium of the model before calculation and complete particle contact during stacking, the tangential stiffness and critical damping were set to 0 during the initial stage of particle stacking equilibrium, with only normal stiffness being applied. Throughout the equilibrium process, the balance of the model was determined by monitoring the distribution of particle contact forces and particle motion velocities. If the ratio-aver was less than  $1e-5$  and the particle velocity was less than 0.001 m/s during the calculation process, the model was considered to be in equilibrium. After the packing of the balls reached equilibrium, the constraints on the pile foundation were released, and parameters such as tangential stiffness and critical damping for the balls were assigned. The simulation was then model solved until ratio-aver  $< 1e-5$ . In this state, the mesh elements of the pile and tunnel moved in conjunction with the soil particles, as shown in (Fig. 7b).

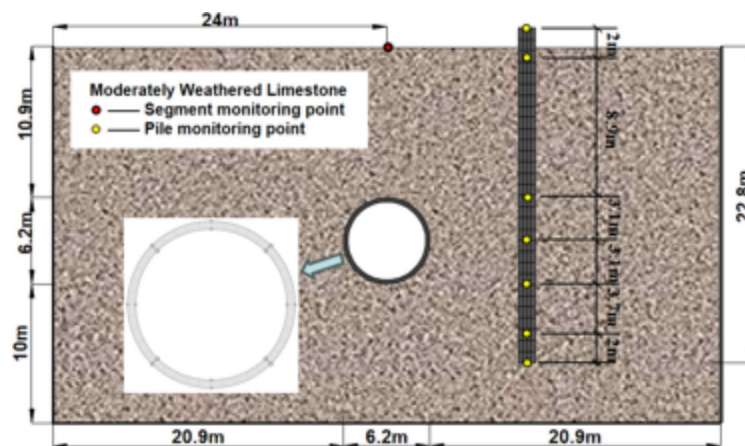
The excavation and support of the tunnel construction were achieved by setting the tunnel as a null model and the tunnel lining segments as an elastic model. The monitored vibration sources were then applied to the tunnel lining segments, allowing for the propagation of vibrations generated during shield tunneling, as shown in (Fig. 7c).

The parameter values used in the simulation were shown in (Table 2). The tunnel segments were modeled as elastic materials, with a density of  $2500 \text{ kg/m}^3$ , a bulk modulus of  $1.917e10 \text{ Pa}$ , and a shear modulus of  $1.438e10 \text{ Pa}$ . The Young's modulus of the pile was set to  $2.25e10 \text{ Pa}$ , with a Poisson's ratio of 0.15.

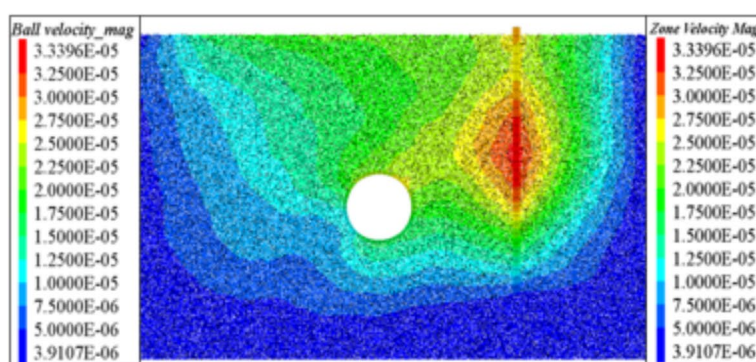
### Model verification

The vibration signal measured on the lining segments at the site was used as the vibration source and input into the segment mesh in the model to simulate the vibration propagation process. Displacement, velocity, and acceleration monitoring points were set up on the model's surface, with the simulation monitoring points shown in (Fig. 7a). A comparison between the numerical simulation results and the ground vibration data collected from the site is presented in (Fig. 8).

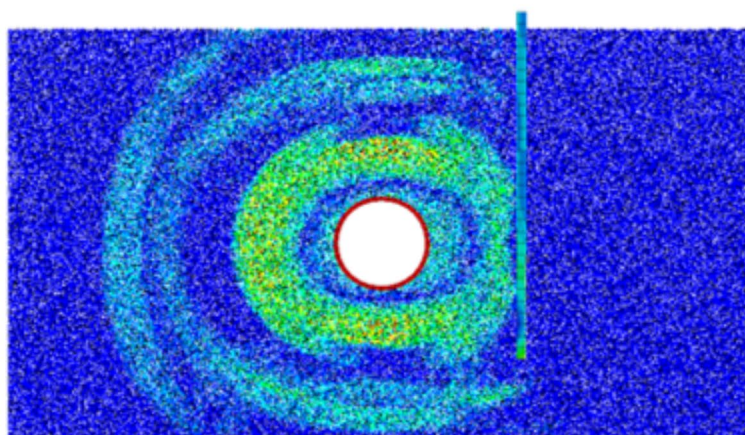
From Fig. 8 it can be observed that the measured and simulated values of the vertical surface vibration displacement directly above the tunnel were primarily within  $\pm 0.02 \text{ mm}$ , with a maximum peak not exceeding  $\pm 0.03 \text{ mm}$ . The measured and simulated values of the vertical surface vibration velocity above the tunnel were mainly within  $\pm 0.3 \text{ mm/s}$ , with the measured data reaching a maximum peak of  $-0.4 \text{ mm/s}$  and the simulated data reaching a maximum peak of  $0.63 \text{ mm/s}$ . The measured values of vertical surface vibration acceleration range between  $\pm 4 \text{ mm/s}^2$ , with a maximum peak of  $7 \text{ mm/s}^2$ , while the simulated values mainly fall within  $\pm 3.5 \text{ mm/s}^2$ , with a maximum peak of  $8.23 \text{ mm/s}^2$ . By comparing the three types of vibration waves, it was evident that the fluctuation range of the vibration acceleration of the numerical model was slightly smaller



(a)



(b)



(c)

**Fig. 7.** Numerical analysis model. (a) Shield tunnel analysis model, (b) Coupled model equilibrium process, (c) Propagation of vibrations during shield tunneling.

stratum type	Density (kN/m <sup>3</sup> )	Emod (Pa)	pb-ten (Pa)	pb-coh (Pa)	krat	fric
Moderately weathered limestone	25	1e5	1e5	1e7	1.5	0.57

**Table 2.** Stratigraphic model parameters.

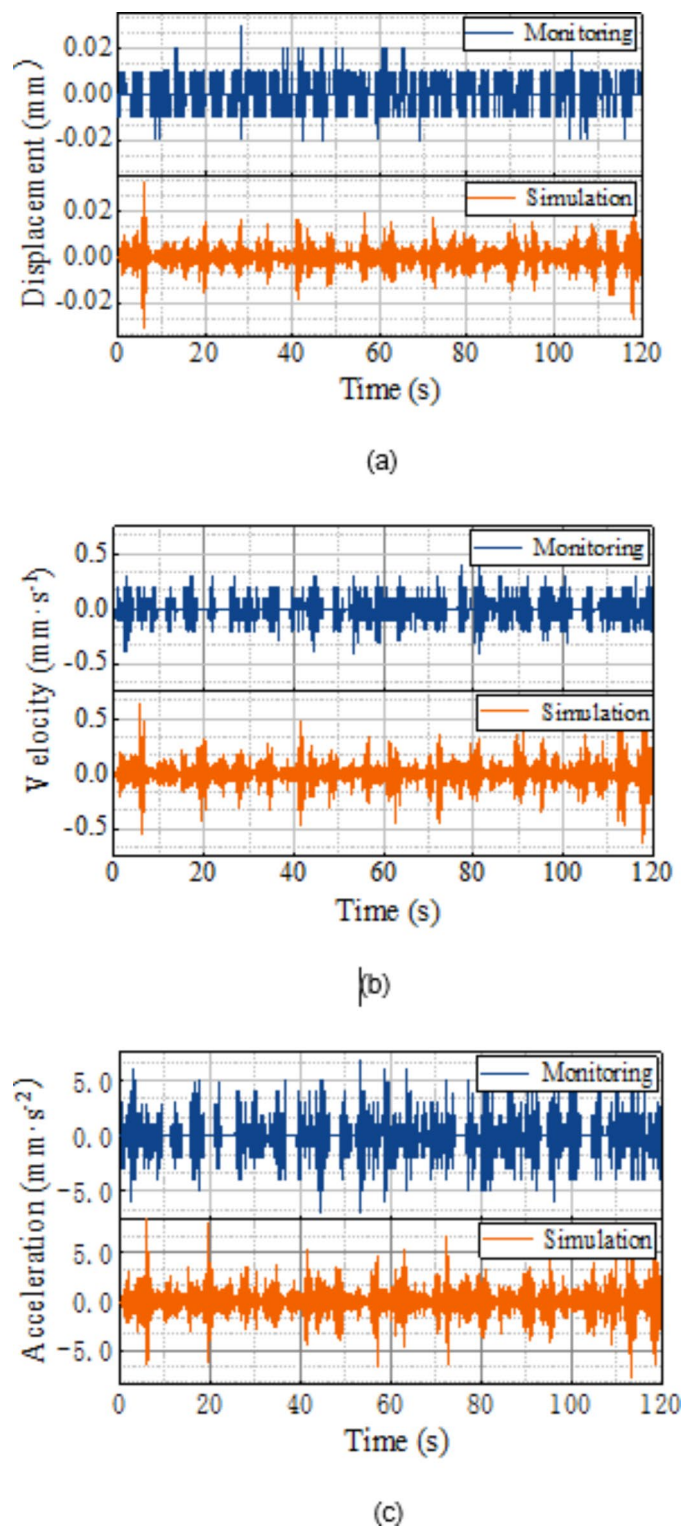


**Fig. 8.** Model verification results. (a) Displacement of ground surface directly above the tunnel, (b) Velocity of ground surface directly above the tunnel, (c) Acceleration of ground surface directly above the tunnel.

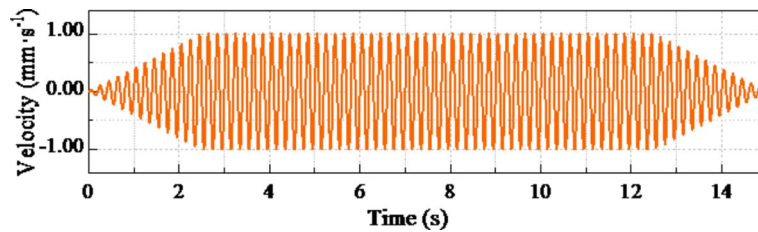


Fig. 9. Simplified vibration source load input.

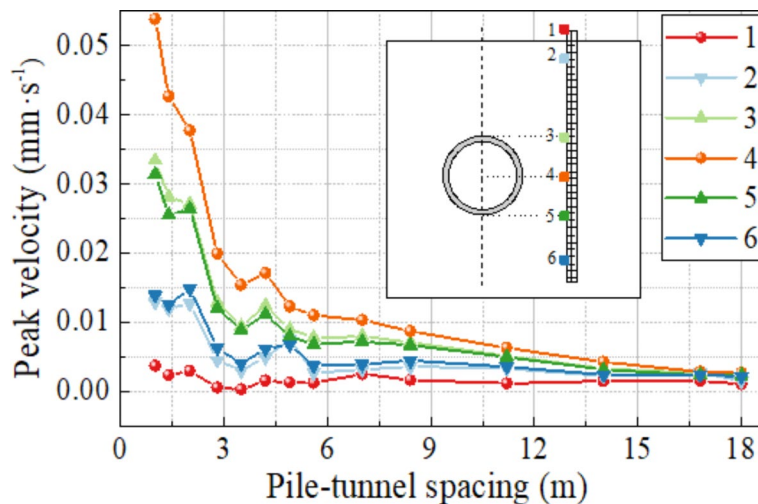


Fig. 10. Peak vibration velocity of pile node.

than the actual values, while the peak velocity was slightly larger. Overall, the measured and simulated data exhibited a generally consistent trend, with smaller differences in peak values and similar vibration intensity. Therefore, it can be concluded that the model was relatively reliable in simulating the propagation of vibrations.

### Numerical results and analysis

In order to explore the influence of shield construction vibration on piles with different pile-tunnel spacing efficiently, based on the vibration source information obtained from field monitoring and analysis, the vibration signal was simplified to a 15s varying load with an amplitude of 1 mm/s and a frequency of 5 Hz as the vibration source input to the model, as shown in (Fig. 9).

### Vibration response results

Figure 10 showed the distribution pattern of vibration velocity peaks at six monitoring points on the pile caused by shield construction vibration at different pile-tunnel spacing. The monitoring points on the pile are labeled from top to bottom as 1, 2, 3, 4, 5, and 6. Among the aforementioned points, monitoring point 1 was situated at the top of the pile, monitoring point 4 was at the same depth as the center of the tunnel, and monitoring points 3 and 5 were respectively at the same depth as the tunnel top and bottom. The depth of monitoring points 2 and 6 were located at 2 m from the top and bottom of the tunnel respectively.

In general, a larger pile-tunnel spacing correlated with reduced vibration response. Within the range of 1–18 m, the maximum peak velocity was recorded at 0.0539 mm/s. However, this peak velocity did not decrease uniformly with increasing spacing. Rather, there was a significant decrease of approximately 60% within approximately 3.5 m. Subsequently, a rebound peak was observed within the range of 3–6 m. Following this, a second minor rebound in velocity peak was observed within the range of 6–9 m. Ultimately, beyond the 12 m threshold, the overall pile vibration velocity was minimal, indicating a trend toward stabilization.

Figure 10 shows that the highest peak of vibration velocity on the pile occurred at monitoring point 4, followed by points 3 and 5, then 2 and 6, with point 1 registering the lowest velocity. Moreover, the vibration velocity at monitoring point 1, located at the pile's apex, appeared less affected by the spacing between the pile and tunnel. However, its trend closely resembled that of the other monitoring points.

Figure 11 depicted the curve of the peak vibration acceleration of piles induced by shield tunneling vibration as a function of the pile-tunnel spacing. The arrangement of monitoring points was consistent with the previous section.

From Fig. 11, it can be observed that the trend of the peak vibration acceleration values at various measurement points with the pile-tunnel spacing followed a similar pattern to that of the vibration velocity. There was an

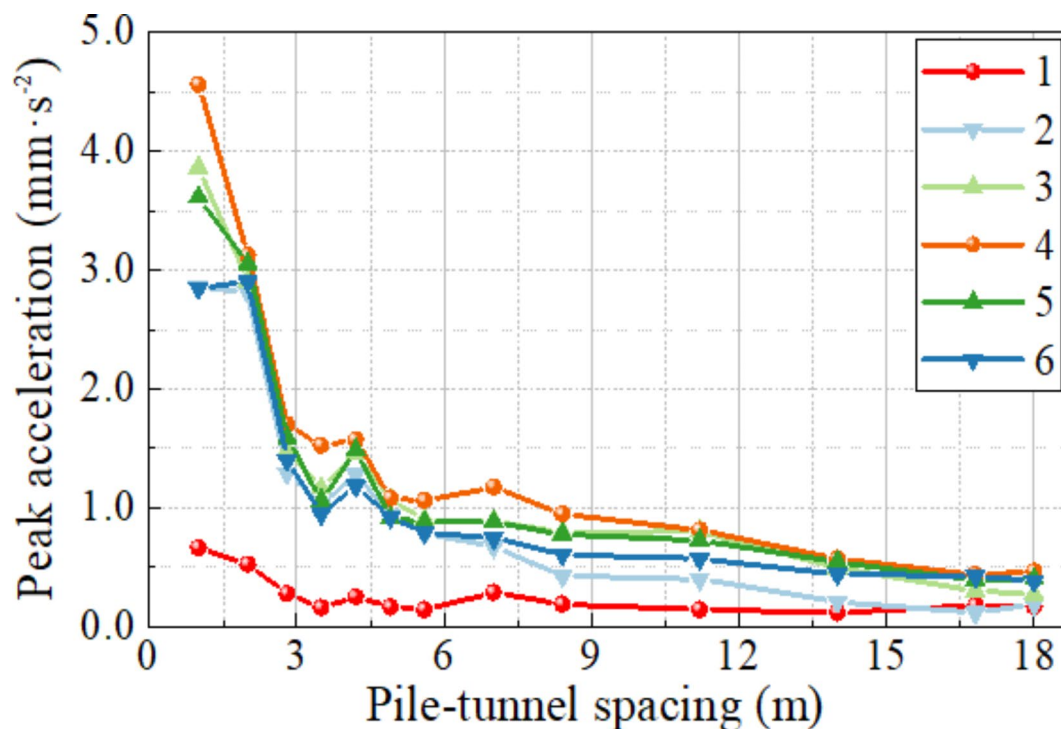


Fig. 11. Peak vibration acceleration of pile node.

abrupt decrease of approximately 60% within a range of approximately 3 m, followed by two distinct rebound peaks occurring within the range of 3–9 m. Finally, beyond the 12 m, the vibration acceleration decreased to approximately  $0.002 \text{ m/s}^2$  and stabilizes.

By analyzing the results of peak vibration velocity and acceleration of the piles, the vibration effect range can be categorized into four segments based on the pile-tunnel spacing: strong (< 3 m), moderate (3–9 m), medium (9–12 m), and weak (> 12 m).

Based on the analysis above, it was evident that monitoring points 2, 6, and 3, 5 exhibited symmetrical positions relative to the tunnel center at point 4. Examination of the vibration acceleration of the piles revealed that the peak velocity and acceleration values at monitoring points 2, 6, and 3, 5 were respectively similar under identical pile-tunnel spacing conditions. Additionally, monitoring point 4 demonstrated a stronger vibration response compared to points 3, 5, with points 3, 5 exhibiting stronger response than points 2, 6. Therefore, it can be inferred that the vibration response pattern of the piles followed an almost symmetrical distribution about the same horizontal line at the depth of the tunnel center, with decreasing vertical vibration response observed as the distance from the vibration source increased.

### Spectrum analysis

#### Fast fourier transform (FFT) analysis

In order to perform a more detailed analysis of the frequency composition of the vibration signals and to obtain the main vibration frequency parameters reflecting the vibration characteristics, the vibration acceleration time-frequency curves of the pile were selected for four different pile-tunnel distances (0.5d, 1d, 1.5d, and 2d, where d is the tunnel diameter). Fast fourier transform (FFT) was applied to the time-domain vibration acceleration signals. This transformation converted the time domain signals to frequency domain signals and produced the corresponding frequency domain curve (Fig. 12). This allowed the frequency domain characteristics of the vibration signal to be analyzed and provides the primary vibration frequency parameter that reflects the vibration frequency characteristics.

Figure 12 displayed the spectral curves of four different pile-tunnel spacing conditions (0.5d, 1d, 1.5d, and 2d). The frequency corresponding to the peak value of the waveform was referred to as the fundamental frequency, and the values on the vertical axis reflected the intensity of each frequency. Figure 12 showed that the frequencies of piles induced by shield tunneling were within the 250 Hz range, with the fundamental frequency concentrated in the 50 Hz range. And for different pile-tunnel spacing conditions, the fundamental frequency of the piles remains the same. This indicated that the fundamental frequency of piles was relatively stable, maintaining within a relatively fixed low-frequency range, without significant changes due to variations in pile-tunnel spacing. Additionally, the amplitude of vibrations gradually decreased as the pile-tunnel distance increased, indicating that the intensity of the vibration signals weakened with increasing pile-tunnel distance.

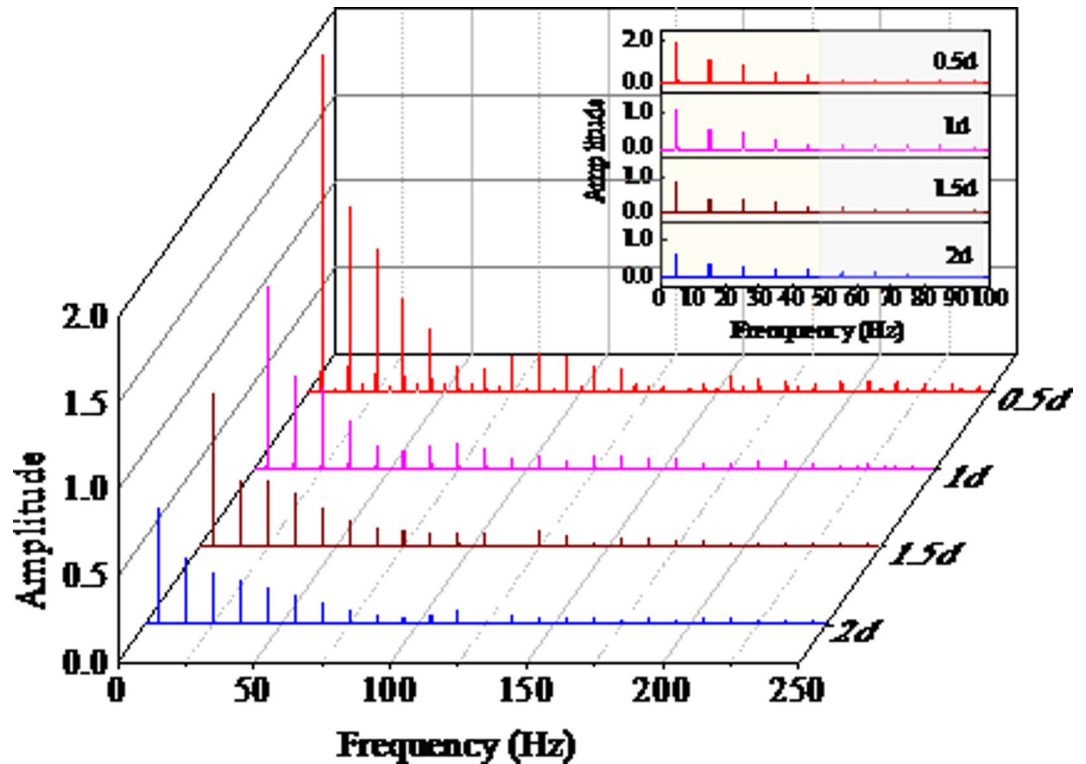


Fig. 12. Vibration spectrum curves of pile (0.5d, 1d, 1.5d and 2d).

#### Wavelet (CWT) and wavelet packet transform analysis

Continuous Wavelet Transform (CWT) and Wavelet Packet Transform (WPT) are effective methods for analyzing the local characteristics of non-stationary signals. They facilitate the decomposition of signals into various frequency components and offer a combined representation of signals in both the time and frequency domains.

The Continuous Wavelet Transform (CWT) is a method of wavelet transformation that operates on a continuous scale. It analyzes the time-frequency characteristics of signals by convolving the signals with continuous wavelet functions at different scales. The morce wavelet was used as the generating function,  $\psi(t)$ , for time-frequency analysis. For a given signal, the wavelet coefficient can be expressed as a complex conjugate<sup>38</sup>.

$$\psi(t) = e^{-\frac{t^2}{2}} e^{-i\omega_0 t} \quad (14)$$

$$\psi(t) = \sqrt{2\pi} e^{\frac{(s-u)^2}{2}} \quad (15)$$

Programming CWT in MATLAB allows for the acquisition of the wavelet spectrogram energy spectrum of vibration signals, enabling further analysis of the frequency characteristics and energy distribution patterns of the vibration signals, as depicted specifically in (Fig. 13).

In the wavelet spectrogram, the brightness of colors represented the energy intensity of the vibration signals in the frequency-time domain. Brighter regions indicated higher energy, while darker regions indicated lower energy levels. Observing the colors and brightness in the time-frequency plot (Fig. 13), it was evident that the main vibration frequencies under the four conditions remained relatively stable, clustered within the 0–50 Hz range. As the propagation distance increased, the dominant frequencies gradually decreased, accompanied by a reduction in the maximum energy value. Additionally, higher frequency components of the vibration signal were significantly attenuated, resulting in a prevalence of low-frequency characteristics in the spectrum plot. This indicated that vibration signals induced by shield tunneling predominantly consisted of low-frequency components, with this portion of vibration propagating over longer distances, exhibiting higher energy levels and slower attenuation. Therefore, due to their broader effect range, careful attention should be given to these vibrations in engineering projects.

The acquired signal was divided into multiple frequency bands by employing wavelet packet decomposition, delineating both high-frequency and low-frequency components. The corresponding signal components of each sub-band were depicted in (Fig. 14). As a result, the characteristic information of the original signal was distributed across the signals of each sub-band. The frequency-domain features of various signals can be quantitatively analyzed and identified based on the energy of each frequency band, as demonstrated in (Fig. 15).

Based on the analysis of the energy distribution across different frequency bands in Fig. 15, it was evident that more than 65% of the vibration energy was concentrated within the low-frequency range of 0–16 Hz. The energy

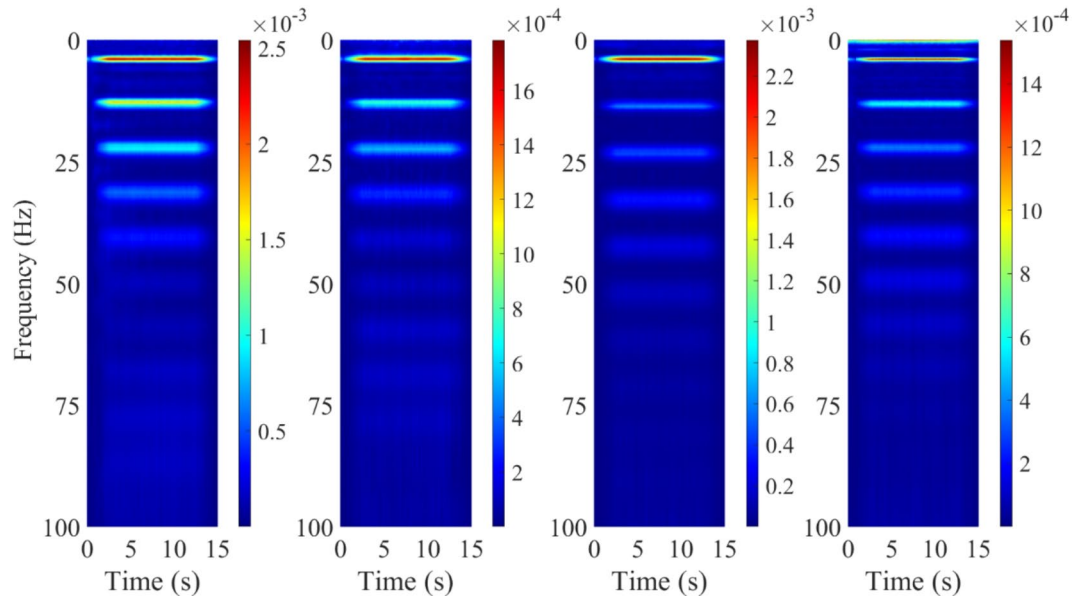


**Fig. 13.** Wavelet spectra of pile monitoring points. (0.5d, 1d, 1.5d and 2d).

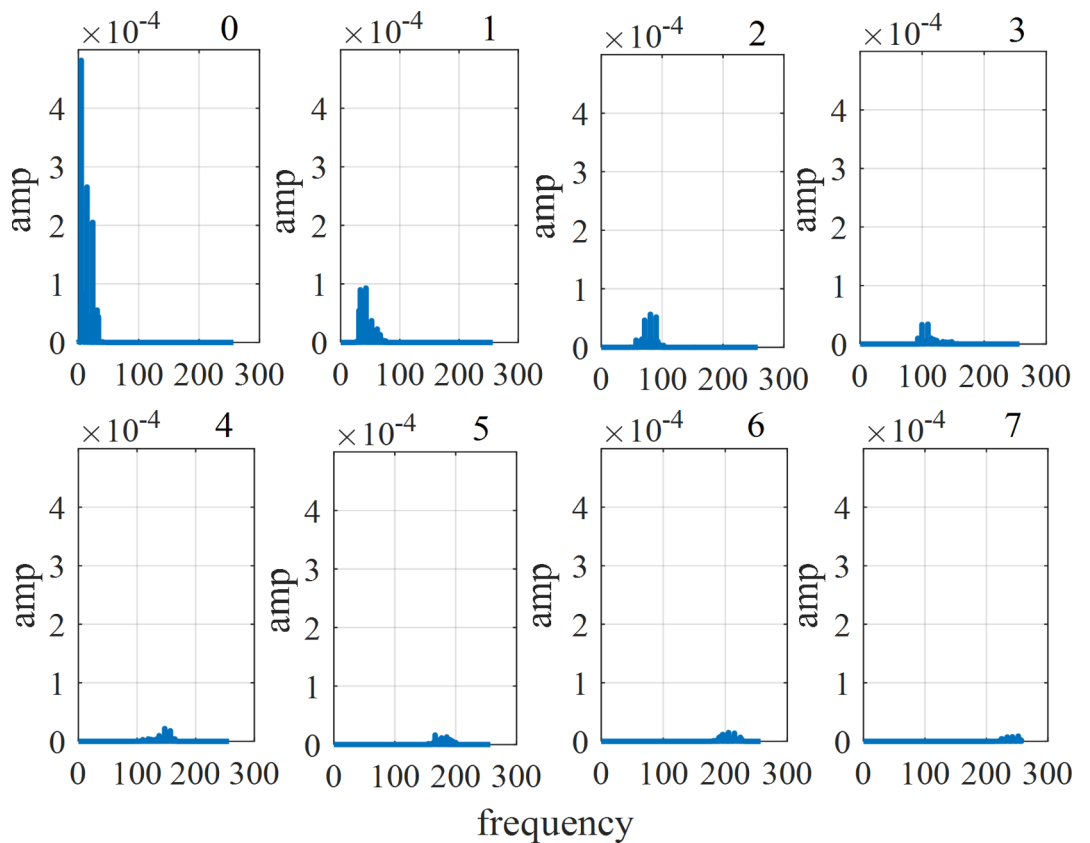


**Fig. 14.** Spectrum of the 8th node in the 3rd layer of the reconstructed signal.

contribution in the 16–32 Hz frequency band was approximately 15%, while it ranged from 5 to 10% in the 32–48 Hz band, and approximately 1–5% in the 48–64 Hz band. For frequency bands above 64 Hz, the energy contribution in each band was less than 1%. This indicated that the vibration energy induced by shield tunneling construction was predominantly concentrated in the low-frequency range. Moreover, vibrations within the 50 Hz frequency range exhibited the most significant effect on the piles.

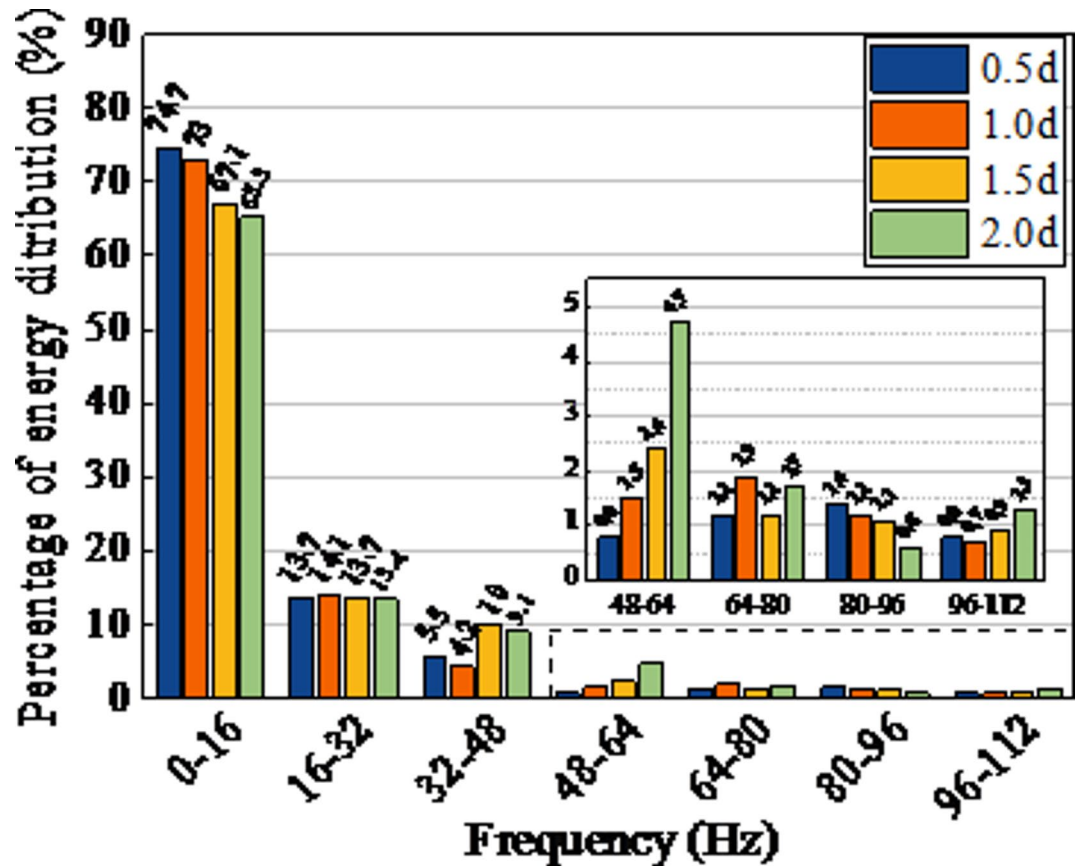


Fig. 15. Percentage distribution of energy in different frequency bands.

This phenomenon can be attributed to the fact that low-frequency vibrations had longer wavelengths and higher energy density. As a result, the vibration waves experienced less absorption or attenuation during propagation, which facilitated easier transmission of vibration energy to surrounding structures and caused a greater effect. This was especially significant for structures such as pile foundations, which typically had lower natural frequencies that aligned with the low-frequency vibration signals induced by shield tunneling. Consequently, they were more susceptible to vibration influences.

Therefore, during shield tunneling operations, it is crucial to carefully consider the influence of low-frequency vibrations on adjacent pile foundations. Correspondingly, appropriate control measures should be implemented to mitigate any adverse effects on nearby structures and infrastructure, thus ensuring the safety and stability of the construction process. Potential strategies may involve adjusting the operational parameters of the shield tunneling equipment and employing vibration attenuation devices to minimize the environmental effect of vibrations on the surroundings.

### Hysteresis curve analysis

Figure 16 depicted the relationship between force and displacement at the pile monitoring points under four different pile-to-tunnel spacing conditions (0.5d, 1d, 1.5d, and 2d). Specifically, Fig. 16a presented the force-displacement curve for monitoring point 3 on the pile; Fig. 16b illustrated the force-displacement curve for monitoring point 4 on the pile; and Fig. 16c showed the force-displacement curve for monitoring point 5 on the pile.

The horizontal axis of Fig. 16 represented the displacement of the pile monitoring points. Figure 16a,b showed that as the pile spacing increased from 0.5d to 1d, the pile displacement decreased from 0.004 mm to 0.002 mm. Furthermore, as the pile-tunnel spacing increased again, the displacement slowly decreased. Figure 16c indicated that within the range of 1d, the pile displacement decreased from 0.003 mm to 0.002 mm and slowly decreased as the pile-to-tunnel spacing increased. This suggested that the vibration induced by shield tunneling significantly affected the piles' displacement within the 1d range of pile-tunnel spacing. Beyond this range, the displacement of the piles was less affected. This phenomenon arose because the pile acted as a reflection point for vibrations when the distance was closer, resulting in repeated propagation of vibration energy between the pile and the tunnel, thereby amplifying its effect on the pile.

From the three graphs in Fig. 16, it can be seen that the force and displacement of the piles exhibited a hysteresis relationship under the cyclic loading of the vibrations generated by the shield tunnel construction. The shape of the hysteresis loop can generally be classified into four types: trapezoidal, arched, reverse S-shape, and Z-shape. The shape of the hysteresis curve provides insight into the variation of the structural stress state.

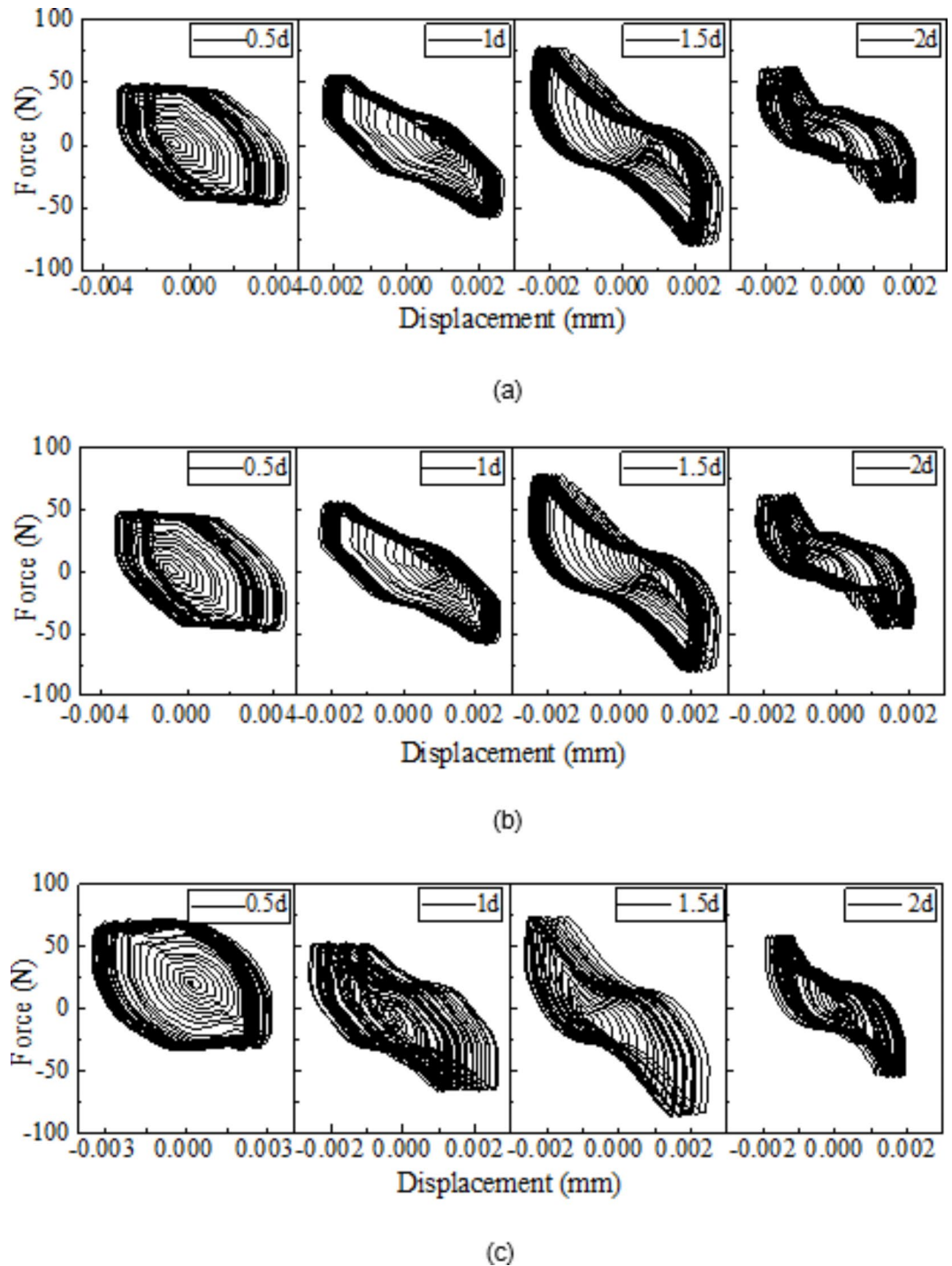


**Fig. 16.** Pile force-displacement curve. (a) Force-displacement curve at monitoring point 3 of pile, (b) Force-displacement curve at monitoring point 4 of pile, (c) Force-displacement curve at monitoring point 5 of pile.

As shown in Fig. 16a, as the pile-tunnel spacing increased from 0.5d to 2d, the shape of the hysteresis curve transformed from a complete trapezoidal to a gradually constricting arched. Figure 16b,c exhibited similar patterns to those in (Fig. 16a). It indicated that the pile changed from a flexural member to a flexural-shear member. It indicated that the pile changed from a flexural member to a flexural-shear member.

This is due to the fact that at smaller pile-tunnel spacing, vibrations can propagate more directly into the pile, inducing bending effects. Since the strain generated by vibrations within the pile mainly occurs along its longitudinal direction, and with the action of vibrations, the pile undergoes bending deformation, resulting in the primary form of stress being bending force. Additionally, smaller pile-tunnel spacing implied less damping and attenuation of vibrational energy during propagation, allowing vibrations to influence the bending deformation of the pile more significantly.

As the pile-tunnel spacing increases, the distribution of vibration energy received in the pile becomes more uniform due to the extended propagation distance of the vibration. Consequently, the vibration energy disperses more evenly within the pile, rather than being concentrated at the top or bottom. Instead, it is uniformly distributed along the transverse direction of the pile. This phenomenon results in a gradual escalation of shear forces exerted on the pile and a corresponding rise in shear stress induced within the pile due to vibration. Therefore, with the increasing pile-tunnel spacing, the shear forces acting on the pile gradually increase, while the bending forces decrease accordingly.

The hysteresis relationship essentially describes the characteristics of energy loss. The area of the resulting hysteresis loop indicates the amount of energy dissipated by the structure. According to the results in Fig. 16a,b, the area of the hysteresis loop decreased as the pile spacing increased, with the most significant reduction occurring within the range of 0.5d to 1d. It suggested that within the 1d pile-tunnel spacing range, the energy fluctuations of the pile were more evident, with a greater effect of vibration. A comprehensive comparative analysis of the four conditions revealed an increase in pile energy dissipation as the pile-tunnel spacing decreased. This trend could be attributed to the reduced propagation distance of vibration with decreasing pile-tunnel spacing, fostering enhanced interaction between the pile and the tunnel. These interactions expedited the conversion of vibrational energy into heat or other forms, thus accelerating the process of energy dissipation.

### Engineering field analysis

According to the environmental profile of the Shanshan section of Jinan Metro Line 4, the horizontal distance between the Wendong 3# residential building and the tunnel is only 2.34 m, making it susceptible to construction vibrations. To assess the actual impact of shield tunneling vibration on adjacent piles, the on-site monitoring data from the start-up of the shield machine to the official excavation process (Fig. 17) were selected as the vibration input of the numerical model, which was loaded on the tunnel lining structure to carry out the dynamic response of piles.

### Vibration acceleration

Based on the overview of adjacent structures to the project, piles located at a distance of 2.34 m from the tunnel was established for preliminary vibration response analysis, and the vibration acceleration was obtained as shown in (Fig. 18).

From Fig. 18, it can be observed that the vibration response was relatively minor in the initial 20 s following the commencement of the shield machine. The maximum acceleration during the shield tunneling phase between 20 and 100 s reached  $6 \text{ mm/s}^2$ . The vibration peak velocity of piles exhibited a periodic pattern, with a slight lag behind the vibration source wave. The intensity and peak values of pile vibration acceleration gradually increased throughout the process as the shield advanced, with a higher frequency of peak occurrences between 80 and 100 s. This indicated that the vibration response of the piles increased from weak to strong during the period from the start-up of the shield machine to formal excavation, following a trend similar to the intensity of the vibration source. The vibration wave exhibited periodicity, and the vibration response lagged behind the vibration source.

In order to visually represent the spectral characteristics more intuitively, the vibration response signals of the pile were subjected to fast fourier transform (FFT) analysis, resulting in the spectral characteristic curve as shown in (Fig. 19).

From Fig. 9, it can be observed that there were three peaks below 150 Hz, with the first two peaks being much sharper than the third peak. Above 150 Hz, there were no prominent peaks in the vibration waves and the amplitudes were relatively small. Consequently, it can be concluded that the first modal frequency of the pile

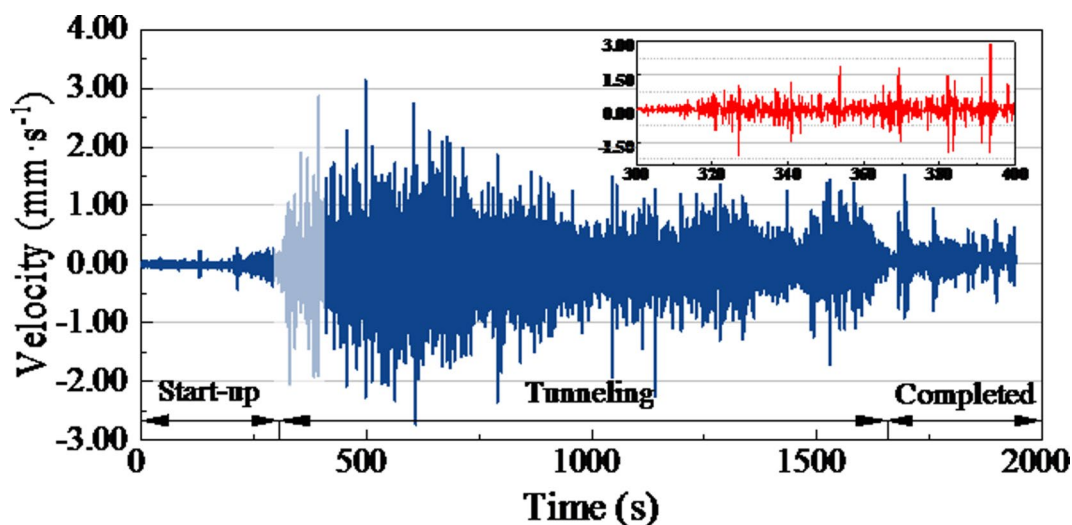


Fig. 17. Monitoring data of vibration velocity of the first segment of tunnel lining.

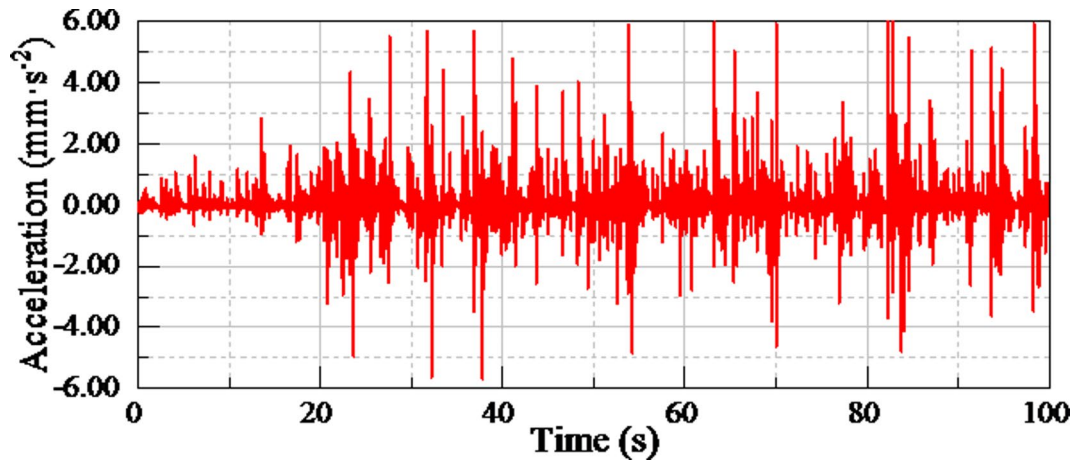


Fig. 18. Vibration acceleration of piles at 2.34 m from tunnel.

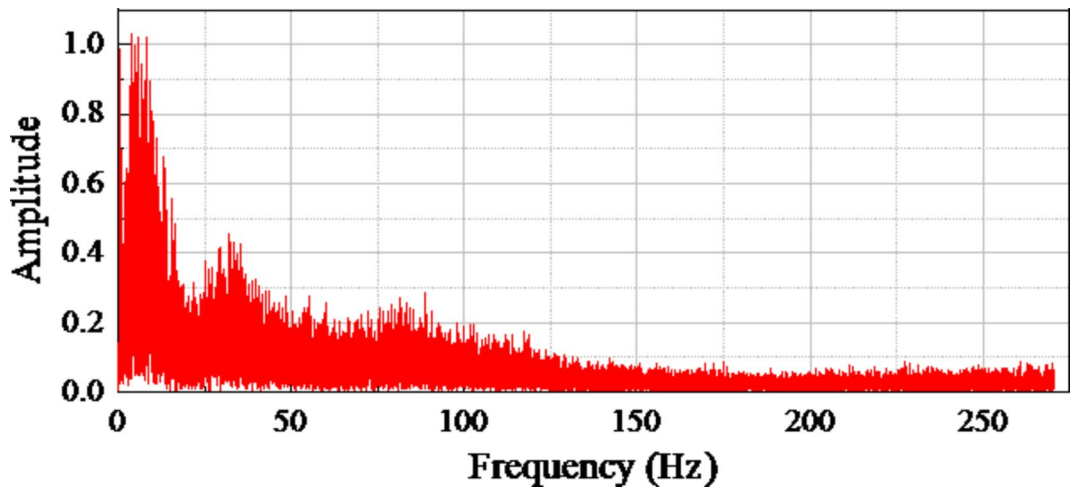


Fig. 19. Spectral curve of piles at 2.34 m from tunnel.

at a distance of 2.34 m caused by shield tunneling construction was approximately 4.94 Hz, the second modal frequency was approximately 32.08 Hz, and the third modal frequency was approximately 81.4 Hz.

It was consistent with the conclusion drawn in the previous section, which indicated that the vibration waves induced by shield tunneling were predominantly low-frequency and propagated further at lower frequencies, thereby exerting a greater impact on nearby structures.

### Vibration level

The project traversed a densely populated area of the main city, with many buildings in the vicinity. The tunnel was shallowly buried and had a long construction period. Shield tunneling will have a significant effect on nearby buildings and residents. According to the 《Standard of vibration in urban area environment》 GB 10071-88, the vibration acceleration level VL<sub>z</sub> was defined as:

$$VL_z = 20 \lg(a_{rms}/a_{ref}) \tag{16}$$

VL<sub>z</sub>— Vibration acceleration level, dB;

a<sub>0</sub>— Reference acceleration, with a value of 10<sup>-6</sup>m/s<sup>2</sup>. Whereas, the effective value (rms) is defined according to the standard as:

$$a_{rms} = \sqrt{\frac{\int_0^T a^2(t)dt}{t_m}} \tag{17}$$

a<sub>rms</sub>— Effective acceleration value, m/s<sup>2</sup>;

a(t)— Acceleration at time t, m/s<sup>2</sup>;

Pile-tunnel spacing/m	$a_{rms}/mm\cdot s^{-2}$	VLz/dB
1.4(0.25d)	7.79E-03	77.83
2.8(0.5d)	7.53E-03	77.54
4.2(0.75d)	7.07E-03	76.99
5.6(1.0d)	6.91E-03	76.78
8.4(1.5d)	7.03E-03	76.93
11.2(2.0d)	6.07E-03	75.67
16.8(3.0d)	5.02E-03	74.02
17.9(3.2d)	4.68E-03	73.41
19.6(3.5d)	3.92E-03	71.87

**Table 3.** Effective values acceleration and seismic intensity.

$t_m$  — Duration of vibration, s;

The effective value acceleration and vibration level within 20 m of the tunnel can be calculated according to Eqs. (16) and (17), as shown in (Table 3).

According to the “Standard of vibration in urban area environment” (GB 10071-88), the standard values of vibration acceleration level in the Z-direction for residential and cultural/educational areas are 67 dB for both day and night. It is not permissible for the nighttime level to exceed the standard by 3 dB.

As shown in Table 3, the vibration level decreased with the increased distance from the tunnel. However, the vibration effects were higher within the range of 1.5d (8.4 m), and the vibration levels within 20 m from the tunnel exceeded 70dB, with a maximum of 77.83dB, surpassing the night-time vibration level required for residential areas. Consequently, it is necessary to control the construction schedule and conduct research on construction vibration, focusing on nearby structures within the range of 1.5d (8.4 m), to propose effective vibration and noise reduction measures.

## Conclusion

This study established the tunnel structure-rock-pile numerical model with different pile-tunnel spacing working conditions based on the field monitoring and DEM-FDM coupling method. To investigate the effects of vibration caused by shield tunnel construction on various ranges of piles. The vibration response law of piles with different pile-tunnel spacing was summarized through the time domain, frequency domain, and energy analysis methods. The following conclusions were drawn:

- (1) With increasing pile-tunnel spacing, the vibration response of the pile diminishes. However, a peak rebound phenomenon occurs within a certain range (3–9 m). The influence range is categorized into four parts based on varying pile-tunnel spacing: intense (<3 m), moderate (3–9 m), medium (9–12 m), and weak (>12 m).
- (2) The primary vibration frequencies of piles induced by shield tunneling fall within the range of 5–50 Hz for various pile-tunnel spacing. Furthermore, the predominant low-frequency nature of these vibration signals is observed, with the high-frequency components decreasing as the pile-tunnel spacing increases. The low-frequency vibrations propagate over longer distances, resulting in a broader effect range.
- (3) The vibration energy induced by shield tunneling mainly accumulates within the low-frequency band. Within the same vibration signal, higher-frequency components contain lower energy. Vibration signals within the 50 Hz frequency range exhibit the highest energy levels, resulting in the most significant effect on the piles.
- (4) Within a 1d distance range between the pile and the tunnel, the vibration induced by shield tunneling significantly affected the displacement and energy variation of the pile. Furthermore, as the pile-tunnel spacing increases, the piles transition from being subjected to bending to experiencing bending-shear forces.

Overall, the dynamic response of surrounding pile foundations to the vibrations generated by shield tunneling cannot be overlooked. Attention should be paid not only to nearby buildings and sensitive structures but also to buildings with low natural frequencies and those within peak rebound zones. Additionally, for pile foundations within a 20-meter radius, the surface vibration levels exceed the regulatory limits for residential areas at night, necessitating control over construction times. The results of this study can offer practical recommendations for engineering applications and provide a reference for future research on vibrations related to shield tunneling. Further experimental investigation on the peak rebound zones during the vibration propagation process of shield tunneling.

## Data availability

The datasets used and/or analysed during the current study available from the corresponding author on reasonable request.

Received: 18 May 2024; Accepted: 12 September 2024

Published online: 17 September 2024

## References

- China, M. o. T. o. t. P. s. R. o. November 2023 Urban Rail Transit Operation Data Report., (2023).
- Agrawal, A. K., Murthy, V. & Chattopadhyaya, S. Investigations into reliability, maintainability and availability of tunnel boring machine operating in mixed ground condition using Markov chains. *Eng. Fail. Anal.* **105**, 477–489 (2019).
- Liu, Q. et al. Research advances of tunnel boring machine performance prediction models for hard rock. *Chin. J. Rock. Mech. Eng.* **35**, 2766–2786 (2016).
- Wei, G., Jiaqing, D. & Long, Y. Numerical analysis on impact of vibration on surrounding environment in TBM construction of subway tunnel. *Subgrade Eng.*, 100–103 (2015).
- Jiancai, Z., Zhibao, D., Fengfeng, Y., ZONGhao, Y. & Zhe, W. Investigations on main influencing factors on vibrations of tunnel boring machine in composite ground. *J. Zhejiang Univ. Technol.* **50**, 435–443 (2022).
- Zhang, Z. & Chou, W. Study of the zones influenced by the construction of metro running tunnels approaching existing buildings. *Mod. Tunn. Technol.* **53**, 075–082 (2016).
- Xing, X. et al. Assessment of noise annoyance level of shield tunneling machine drivers under noisy environments based on combined physiological activities. *Appl. Acoust.* **179**, 108045 (2021).
- Zhigeng, J. & Wei, L. Environmental impact and countermeasure study on construction time of underground 1 project in Shenyang. *Environ. Prot. Sci.* 67–70. <https://doi.org/10.16803/j.cnki.issn.1004-6216.2006.01.021> (2006).
- Guo, F., Huang, J., Su, Y., Bian, J. & Xu, Q. Shield Construction process Induced Vibration source characteristics. *J. Beijing Univ. Technol.* **40**, 1820–1827 (2014).
- yajun, D. Vibration control and monitoring analysis of shield tunnel side crossing the museum on Changsha Metro line 6. *Mod. Urban Transit.*, 93–97 (2019).
- Nelson, P., O'Rourke, T., Flanagan, R., Kulhawy, F. & Ingraffea, A. *Tunnel Boring Machine Performance Study. Final Report.* (United States) (Urban Mass Transportation Administration, 1984).
- Namli, M. & Aras, F. Investigation of effects of dynamic loads in Metro tunnels during construction and operation on existing buildings. *Arab. J. Geosci.* **13**, 424 (2020).
- Haowen, T. Safety guarantee measures for intermediate floor slab of metro station when TBM passing. *Tunn. Constr.*, 129–134 (2013).
- Wu, J. et al. Attenuation characteristics of impact-induced seismic wave in deep tunnels: an in situ investigation based on pendulum impact test. *J. Rock Mech. Geotech. Eng.* **14**, 494–504 (2022).
- Guo, F. et al. Analysis of propagation and attenuation of vibration induced by shield tunneling in Lanzhou sandy gravel layer. *Rock. Soil. Mech.* **39**, 3377–3384 (2018).
- Wu, K. et al. Vibration response law of existing buildings affected by subway tunnel boring machine excavation. *Tunn. Undergr. Space Technol.* **120**, 104318 (2022).
- Liu, M. B. et al. *Field Monitoring of TBM Vibration during Excavating Changing Stratum: Patterns and Ground Identification* 1–18 (Rock Mechanics and Rock Engineering, 2022).
- Riqing, X. et al. Overview on influence of vibration Induced by shield construction on adjacent buildings and its control measures. *Tunn. Constr.* **41**, 14–21 (2021).
- Xin, W., Xuan, H., Honglei, Z. & Chonghong, L. Numerical simulation on vibration response of surrounding ancient buildings induced by shield tunneling: Case study on line 8 of Beijing metro. *Tunn. Constr.* **33**, 6 (2013).
- Xin, W., Xuan, H. & Honglei, Z. Research on environment vibration response induced by metro shield tunneling in central urban area. *China Civil Eng. J.*, 309–314 (2015).
- Xin, W., Xuan, H., Honglei, Z. & Chonghong, L. Numerical simulation study on ground vibration response induced by metro shield construction. *Chin. J. Undergr. Space Eng.* **11**, 1552–1557 (2015).
- Jing-yue, W. et al. Numerical simulation of vibration induced by shield tunneling in liquefiable ground. *Earthq. Resistant Eng. Retrofitting* **45**, 158–167 (2023).
- Hasheminezhad, A. & Bahadori, H. Seismic response of shallow foundations over liquefiable soils improved by deep soil mixing columns. *Comput. Geotech.* **110**, 251–273 (2019).
- Gupta, S., Stanus, Y., Lombaert, G. & Degrande, G. Influence of tunnel and soil parameters on vibrations from underground railways. *J. Sound Vib.* **327**, 70–91 (2009).
- Lu, Z., Wang, X., Zhou, G., Feng, L. & Jiang, Y. Investigation on vibration influence law of double-shield TBM tunnel construction. *Appl. Sci.* **12**, 7727 (2022).
- Guo, F., Yi, S., Lianjin, T. & Jun, H. Shield tunneling lnduced vibration on frame structure Impact study. *Constr. Technol.*, 105–109 (2015).
- Yang, S. & Jia, M. ALEM-FEM-BEM coupling for response analysis of pile group in laminated fluid-saturated geomaterials induced by tunnel excavation. *Constr. Build. Mater.* **442**, 137602 (2024).
- Lai, J. et al. Shield-driven induced ground surface and Ming Dynasty city wall settlement of Xi'an Metro. *Tunn. Undergr. Space Technol.* **97**, 103220 (2020).
- Chao, Z., Qing-song, F. & Wei, H. Research review on environmental vibrations in metro depot and over-track buildings induced by train operation. *J. Traffic Transp. Eng.* **23**, 27–46 (2023).
- Qingsong, F., Xiaoyan, L. & Songliang, L. A. Review of researches on environmental vibration induced by high-speed trains. *J. East. China Jiaotong Univ.* **25**, 1–5 (2008).
- Ma, L. & Liu, W. LIU, W.-f. Sliced finite element-infinite element coupling model for predicting environmental vibration induced by metro train. *Chin. J. Rock Mechan. Eng.* **35**, 2131–2141 (2016).
- Jin, Q., Thompson, D. J., Lurcock, D. E. & Ntotsios, E. The shadow effect on the ground surface due to vibration transmission from a railway tunnel. *Transp. Geotech.* **23**, 100335 (2020).
- Seo, H. Infrared thermography for detecting cracks in pillar models with different reinforcing systems. *Tunn. Undergr. Space Technol.* **116**, 104118 (2021).
- Yan, B., Wang, R., Ding, B., Dai, F. & Wang, Y. Numerical simulation analysis of tunnel backfill grout based on DEM-FDM coupling and particle inlet. *Undergr. Space* **14**, 285–299 (2024).
- Wang, T., Han, Y., Han, Y. & Zhang, F. *PFC2D/3D Particle Discrete Element Method and Applications* (China Architecture & Building, 2020).
- Chong, S., Qiang, Z. & Shengnian, W. Granular Flow (PFC5.0) Numerical Simulation Techniques and Applications. (2018).
- Cundall, P. & Manual, P. U. Itasca Consulting Group Inc. PFC3D version 6 (2004).
- Chen, C., Seo, H. & Zhao, Y. A novel pavement transverse cracks detection model using WT-CNN and STFT-CNN for smartphone data analysis. *Int. J. Pavement Eng.* **23**, 4372–4384 (2022).

## Author contributions

You Wang: conceptualization, methodology, project administration, supervision, investigation, writing-review and editing; Yue Ma: data curation, writing-original draft, software, visualization; Rui Wang: resources, writing-review and editing, investigation, project administration; Bosong Ding: validation, visualization; Siyuan Yu: investigation, project administration;

## Funding

The research reported in this paper has been funded by the National Natural Science Foundation of China (51778633,51308552); China Railway Construction Corporation 2022 Annual Scientific and Technological Research and Development Plan and Funding Subjects(2022-C1); Science and Technology Research and Development Plan of China Railway Corporation in 2020(41,243); 2022 degrees Guangzhou Metro Design and Research Institute Co. (KY-2022-014); Science and technology research and development plan topics of China Railway Second Bureau Group Co.( 2022-B-4).

## Declarations

### Competing interests

The authors declare no competing interests.

### Additional information

**Correspondence** and requests for materials should be addressed to Y.W.

**Reprints and permissions information** is available at [www.nature.com/reprints](http://www.nature.com/reprints).

**Publisher's note** Springer Nature remains neutral with regard to jurisdictional claims in published maps and institutional affiliations.

**Open Access** This article is licensed under a Creative Commons Attribution-NonCommercial-NoDerivatives 4.0 International License, which permits any non-commercial use, sharing, distribution and reproduction in any medium or format, as long as you give appropriate credit to the original author(s) and the source, provide a link to the Creative Commons licence, and indicate if you modified the licensed material. You do not have permission under this licence to share adapted material derived from this article or parts of it. The images or other third party material in this article are included in the article's Creative Commons licence, unless indicated otherwise in a credit line to the material. If material is not included in the article's Creative Commons licence and your intended use is not permitted by statutory regulation or exceeds the permitted use, you will need to obtain permission directly from the copyright holder. To view a copy of this licence, visit <http://creativecommons.org/licenses/by-nc-nd/4.0/>.

© The Author(s) 2024